Condensates in rotating turbulent flows

Kannabiran Seshasayanan[1]†, and Alexandros Alexakis[1]

[1]Laboratoire de physique statistique, Département de physique de l' École normale supérieure, PSL Research University, Université Paris Diderot, Sorbonne Paris Cité, Sorbonne Universités, UPMC Univ. Paris 06, CNRS, 75005 Paris, France

(Received 18 February 2022; revised xx; accepted xx)

Using a large number of numerical simulations we examine the steady state of rotating turbulent flows in triple periodic domains, varying the Rossby number Ro (that measures the inverse rotation rate) and the Reynolds number Re (that measures the strength of turbulence). The examined flows are sustained by either a helical or a non-helical Roberts force, that is invariant along the axis of rotation. The forcing acts at a wavenumber k_f such that $k_f L = 4$, where $2\pi L$ is the size of the domain. Different flow behaviours were obtained as the parameters are varied. Above a critical rotation rate the flow becomes quasi two dimensional and transfers energy to the largest scales of the system forming large coherent structures known as condensates. We examine the behaviour of these condensates and their scaling properties close and away from this critical rotation rate. Close to the the critical rotation rate the system transitions supercritically to the condensate state displaying a bimodal behaviour oscillating randomly between an incoherent-turbulent state and a condensate state. Away from the critical rotation rate, it is shown that two distinct mechanisms can saturate the growth of the large scale energy. The first mechanism is due to viscous forces and is similar to the saturation mechanism observed for the inverse cascade in two-dimensional flows. The second mechanism is independent of viscosity and relies on the breaking of the two-dimensionalization condition of the rotating flow. The two mechanisms predict different scaling with respect to the control parameters of the system (Rossby and Reynolds), which are tested with the present results of the numerical simulations. A phase space diagram in the Re, Ro parameter plane is sketched.

Key words:

1. Introduction

Turbulent rotating flows are met in a variety of contexts in nature. From the interior of stars, to planet atmospheres and industrial applications, rotation plays a dominant role in determining the properties of the underlying turbulence (Greenspan 1968; Hopfinger & Heijst 1993; Pedlosky 1987). In its simplest form an incompressible turbulent flow in the presence of rotation is controlled by the incompressible Navier-Stokes equation, that in a rotating frame of reference reads:

$$\partial_t \mathbf{u} + \mathbf{u} \cdot \nabla \mathbf{u} + 2\Omega \hat{\mathbf{e}}_\mathbf{z} \times \mathbf{u} = -\nabla P + \nu \Delta \mathbf{u} + \mathbf{F} \tag{1.1}$$

where $\mathbf{u}$ is the incompressible velocity field, Ω is the rotation rate (assumed here to be in the z direction with $\hat{\mathbf{e}}_z$ its unit vector), P is the pressure that enforces the

† Email address for correspondence: skannabiran@lps.ens.fr

incompressibility condition $\nabla \cdot \mathbf{u} = 0$, ν is the viscosity and $\mathbf{F}$ is a mechanical body force that acts at some length-scale ℓ_f. Traditionally the strength of turbulence compared to viscous forces is measured by the Reynolds number $Re = U\ell_f/\nu$, while compared to the Coriolis force it is measured by the Rossby number $Ro = U/(2\Omega\ell_f)$, where U stands for the velocity amplitude. Precise definitions of these numbers will be given when we describe in detail the model under study.

It has been known for some time that when rotation is very strong, flows tend to become quasi-two-dimensional (quasi-2D) varying very weakly along the direction of rotation (Hough 1897; Proudman 1916; Taylor 1917). The reason for this behaviour is that the incompressible projection of the Coriolis force $2\Omega\hat{\mathbf{e}}_\mathbf{z} \times \mathbf{u} - \nabla P' = 2\Omega\Delta^{-1}\partial_z \nabla \times \mathbf{u}$ does not act on the part of the flow that is invariant along the rotation axis $\partial_z \mathbf{u} = \mathbf{0}$. At the same time velocity fluctuations that vary along this axis become inertial waves that satisfy the dispersion relation,

$$\omega_\mathbf{k} = \pm 2\Omega \frac{k_z}{k}, \tag{1.2}$$

where $\omega_\mathbf{k}$ is the wave frequency, $\mathbf{k}$ the wavenumber and the sign depends on the helicity of the mode. Fast rotation leads to a de-correlation of inertial waves weakening their interactions. Thus, in the presence of strong rotation, fluid motions that are invariant along the direction of rotation (often referred as the slow manifold) become isolated from the remaining flow and if forced they dominate leading to the quasi-2D behaviour (Chen *et al.* 2005; Scott 2014). This quasi-2D behaviour has been realized in experiments (Ibbetson & Tritton 1975; Hopfinger *et al.* 1982; Dickinson & Long 1983; Baroud *et al.* 2002, 2003; Sugihara *et al.* 2005; Ruppert-Felsot *et al.* 2005; Morize & Moisy 2006; Staplehurst *et al.* 2008; van Bokhoven *et al.* 2009; Yoshimatsu *et al.* 2011; Machicoane *et al.* 2016) and numerical simulations (Yeung & Zhou 1998; Smith & Waleffe 1999; Godeferd & Lollini 1999; Chen *et al.* 2005; Thiele & Müller 2009; Mininni *et al.* 2009; Mininni & Pouquet 2010; Favier *et al.* 2010; Sen *et al.* 2012; Marino *et al.* 2013; Alexakis 2015; Biferale *et al.* 2016; Valente & Dallas 2017).

These arguments however have various limitations. For large Reynolds numbers Re, the quasi-2D behaviour breaks down at scales ℓ smaller than the Zeman scale ℓ_z defined as the scale for which the vorticity $w_\ell \propto u_\ell/\ell$ is comparable to the rotation rate Ω (Zeman 1994). Here u_ℓ stands for the typical velocity at scale ℓ. Thus for large Re and low Rossby flows, such that $1 \ll 1/Ro \ll Re$, the large scales $\ell > \ell_z$ show a quasi-2D behaviour while smaller scales $\ell < \ell_z$ display three-dimensional (3D) behaviour. Furthermore, the quasi-2D behaviour is also expected to break down even at large scales for sufficiently elongated boxes $H \gg \ell_f$, (where H stands for the domain size in the direction of rotation). If H is sufficiently large, the slowest inertial mode has a frequency $\omega \sim \Omega\ell_f/H$ comparable or smaller to the inverse eddy turnover time ℓ/u_ℓ. This last limiting procedure, $1 \ll 1/Ro \ll H/\ell_f$ provided also that $Re \gg 1$ corresponds to the weak wave turbulence limit, in which the nonlinear interactions can be treated in a perturbative manner Galtier (2003); Nazarenko (2011). Finally, for finite (fixed) heights H and finite (fixed) Reynolds numbers, fast rotating flows become exactly 2D above a critical rotation rate (Gallet 2015). This corresponds to the limiting procedure $Re \ll 1/Ro$ and $H/\ell_f \ll 1/Ro$. Thus, in general, the quasi-2D behaviour at low Ro depends, on the scales under investigation, the geometry of the system, and the relative amplitude of the Rossby and Reynolds number, with different limits leading to different results.

The distinctive difference between 3D and 2D or quasi-2D flows is that the former one cascades energy to small scales while the later one cascades energy to large scales. Thus a significant change in the energy balance occurs when the rotation rate is increased

and the flow becomes quasi-2D: while in a forward cascade the energy that arrives at small scales gets dissipated, in an inverse cascade energy piles up at scales of the size of the domain size L. Indeed it has been shown both in numerical simulations (Smith & Waleffe 1999; Smith *et al.* 1996; Pouquet *et al.* 2013; Sen *et al.* 2012; Deusebio *et al.* 2014; Biferale *et al.* 2016) and experiments (Yarom *et al.* 2013; Campagne *et al.* 2014; Yarom & Sharon 2014; Campagne *et al.* 2015, 2016) that while for weak rotation the flow is close to isotropic state and cascades all energy to the small scales, for fast rotation the flow is in a quasi-2D state that cascades at least part of the energy to the large scales. This change in the direction of the cascade as a parameter is varied has been the subject of study of various investigations in different systems (Smith & Waleffe 1999; Celani *et al.* 2010; Alexakis 2011; Deusebio *et al.* 2014; Sozza *et al.* 2015; Pouquet & Marino 2013; Marino *et al.* 2013; Seshasayanan *et al.* 2014; Marino *et al.* 2015; Seshasayanan & Alexakis 2016; Benavides & Alexakis 2017). In particular for rotating flows it has been shown that the transition from a forward to an inverse cascade happens at critical rotation Ω_c above which the flow starts to cascade part of the injected energy ϵ inversely at a rate ϵ_{inv}. The fraction of the rate that cascades inversely ϵ_{inv}/ϵ depends on the difference $\Omega - \Omega_c$ and the height of the domain H (Deusebio *et al.* 2014) . This description holds at early times before the inverse cascading energy reaches scales the size of the domain. At late times when energy starts to pile up and form a condensate the dynamics might change (Kraichnan 1967; Smith R. & Yakhot 1994; Xia *et al.* 2008).

In this work, we try to determine the behaviour of a forced rotating flow at late times when the flow has reached a steady state, in the absence of any large scale dissipative mechanism. Due to the long computational time required to reach a steady state, very few investigations have focused on this regime like the early low resolution studies in Bartello *et al.* (1994) and more recently the studies in (Alexakis 2015; Dallas & Tobias 2016; Yokoyama & Takaoka 2017), where turbulent rotating flows at steady state were investigated. Experiments on the other hand for which long times are realizable have investigated this steady state limit Campagne *et al.* (2014); Yarom & Sharon (2014); Campagne *et al.* (2016); Machicoane *et al.* (2016).

The rest of this paper is structured as follows. In the next section 2 we present our numerical setup and introduce our control parameters and observables. In section 3 we discuss possible mechanisms for the saturation of the initial energy growth. In section 4 we present the results on global quantities from the numerical simulations and in section 5 we describe the spatial and spectral structures as well the dynamics involved. In the final section 6 we summarize and draw our conclusions.

2. Numerical set-up, and control parameters

We consider the flow of a unit density liquid in a cubic triple periodic domain of size $2\pi L$ that is in a rotating frame with z being the axis of rotation. The governing equation for the flow velocity $\mathbf{u}$ is given by eq. (1.1). The flow is driven by the body force $\mathbf{F}$, here we consider two cases given by,

$$a) \quad \mathbf{F} = f_0 \begin{bmatrix} -\sin(k_f y), \\ +\sin(k_f x), \\ \cos(k_f x) + \cos(k_f y) \end{bmatrix} \quad \text{and} \quad b) \quad \mathbf{F} = f_0 \begin{bmatrix} -\sin(k_f y), \\ +\sin(k_f x), \\ \sin(k_f x) + \sin(k_f y) \end{bmatrix}. \tag{2.1}$$

The first one is maximally helical $\langle \mathbf{F} \cdot \nabla \times \mathbf{F} \rangle_{\mathbf{S}} = \mathbf{k_f} \langle \mathbf{F} \cdot \mathbf{F} \rangle_{\mathbf{S}}$ and will be referred to as the helical forcing and the second one has zero helicity $\langle \mathbf{F} \cdot \nabla \times \mathbf{F} \rangle_{\mathbf{S}} = \mathbf{0}$ and will be referred as the non-helical forcing. Here $\langle \rangle_S$ denotes spatial average. These forcing

functions have been proposed by (Roberts 1972) for dynamo studies and commonly are referred to as Roberts flow. Helicity is known to play an important role in fast rotating turbulence since it has been shown that its forward cascade can control the dynamics at the small scales Mininni & Pouquet (2010); Sen *et al.* (2012). In this work we will examine both cases with and without helicity in parallel. It is also important to note that our forcing is invariant along the axis of rotation and thus the forcing acts only on the slow manifold (that consists of all the Fourier velocity modes for which $k_z = 0$). This in contrast with the case examined in (Alexakis 2015; Yokoyama & Takaoka 2017) where a Taylor-Green forcing was used that has zero average along the vertical direction. Thus, while the Taylor-Green forcing does not inject energy directly to the slow manifold, the Roberts forcing used here injects energy only to the slow manifold. The two cases can thus be considered as two extremes.

This system was investigated using numerical simulations. All runs were performed using the pseudo-spectral code Ghost (Mininni *et al.* 2011), where each component of $\mathbf{u}$ is represented as truncated Galerkin expansion in terms of the Fourier basis. The non-linear terms are initially computed in physical space and then transformed to spectral space using fast-Fourier transforms. Aliasing errors are removed using the 2/3 de-aliasing rule. The temporal integration was performed using a fourth-order Runge-Kutta method. Further details on the code can be found in Mininni *et al.* (2011). The grid size varied depending on the value of Re_F and Ro_F from 64^3 to 512^3. A run was considered well resolved if the value of enstrophy spectrum at the cut-off wavenumber was sufficiently smaller than its value at its peak. Each run started from a random multi-mode initial condition and was continued for sufficiently long time so that long time averages in the steady state were obtained.

The parameter f_0 gives the amplitude of the forcing, and k_f is the wavenumber at which energy is injected into the flow. These two parameters define the length-scale $\ell_f = k_f^{-1}$, the time scale $\tau_f = (k_f f_0)^{-1/2}$ and velocity amplitude $U_f = \sqrt{f_0/k_f}$ which will be used to non-dimensionalize the control parameters in our system. The product $k_f L$ gives the scale separation between the forcing scale and the box size. Throughout this work we have fixed the scale separation to $k_f\, L = 4$. We thus do not investigate the dependence on the box size. The Reynolds number Re_f and the Rossby number Ro_f based on U_f are defined as,

$$Re_f = \frac{\sqrt{f_0/k_f^3}}{\nu} \quad \text{and} \quad Ro_f = \frac{\sqrt{f_0 k_f}}{2\Omega}\,. \tag{2.2}$$

The more classical definition of the Reynolds and Rossby number can be obtained using the root mean square amplitude of the velocity $U = \langle \mathbf{u}\cdot\mathbf{u}\rangle_{ST}^{1/2}$, where $\langle\cdot\rangle_{ST}$ denotes spatial and temporal average. This leads to the velocity based Reynolds number Re_u and the velocity based Rossby number Ro_u,

$$Re_u = \frac{U}{k_f \nu} \quad \text{and} \quad Ro_u = \frac{U k_f}{2\Omega}\,. \tag{2.3}$$

In many experiments as well as in many theoretical arguments it is the energy injection rate

$$\epsilon = \langle \mathbf{u}\cdot\mathbf{F}\rangle_{ST} = \nu \left\langle |\nabla\times\mathbf{u}|^2 \right\rangle_{ST} \tag{2.4}$$

per unit of volume that is controlled. It is thus worth considering expressing the control parameters also in terms of ϵ. This leads to the definition of the Reynolds number based

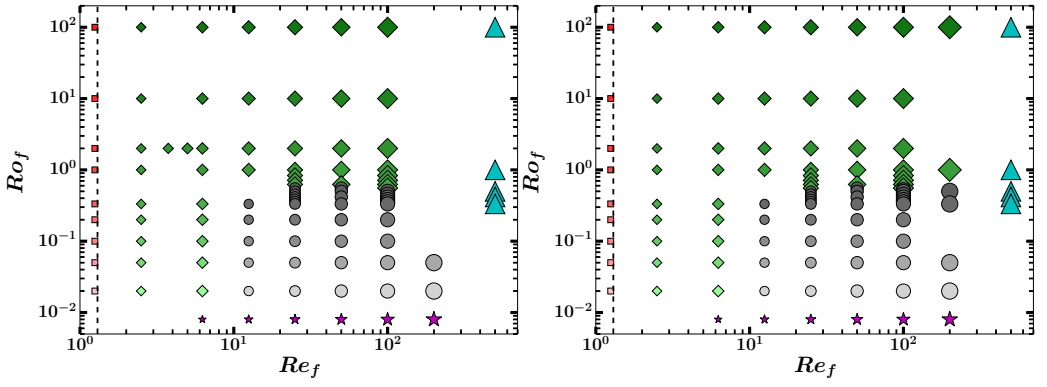

(a) (b)

Figure 1: The figures show the location of all the examined numerical runs in the (Ro_f, Re_f) plane for a) the case of helical flow and b) the case of the non-helical flow. Larger symbols denote larger values of Re_f and lighter symbols correspond to smaller values of Ro_f. Different symbols correspond to different behaviour of the flow.

on ϵ,

$$Re_\epsilon = \frac{\epsilon^{1/3}}{\nu k_f^{4/3}} \quad \text{and} \quad Ro_\epsilon = \frac{\epsilon^{1/3} k_f^{2/3}}{2\Omega}\,. \tag{2.5}$$

Finally, the ratio of the square root of enstrophy to twice the rotation rate is referred to as the micro-Rossby number Ro_λ that in terms of Re_ϵ and Ro_ϵ can be expressed as,

$$Ro_\lambda = \frac{\langle |\nabla \times \mathbf{u}|^2 \rangle_{ST}^{1/2}}{2\Omega} = \frac{\epsilon^{1/2}}{2\nu^{1/2}\Omega} = Re_\epsilon^{1/2} Ro_\epsilon. \tag{2.6}$$

In the examined system only (Re_f, Ro_f) are true control parameters, while (Re_u, Ro_u) and $(Re_\epsilon, Ro_\epsilon)$ can only be measured a posteriori.

The location of all of the performed runs in the (Re_f, Ro_f) parameter space are shown in figure 1 for a) the helical flow, b) the non-helical flow in a log-log scale. The figure shows symbols that correspond to simulations that lead to different hydrodynamic steady states. Darker symbols correspond to larger values of Ro_f while larger symbols correspond to larger values of Re_f. The largest symbols correspond to simulation runs of size 512^3 points. The same symbols, sizes and shades (colours online) are used in some of the subsequent figures and thus the reader can refer to figure 1 to estimate the value of Re_f and Ro_f. Each symbol corresponds to different behaviour of the flow: squares ■ correspond to flows that are laminar, diamonds ♦ correspond to unstable or turbulent flows that do not form a condensate, circles • correspond to turbulent flows that form a condensate. We have shifted the points corresponding to $\Omega = 0, Ro_f = \infty$ to the values $Ro_f = 100$ in order for them to appear along with other points that correspond to finite rotation.

The star symbols ⋆ denote the simulations of the reduced two dimensional equations valid for $Ro_f \to 0$ given by,

$$\begin{aligned} \partial_t \mathbf{u}_{2D} + \mathbf{u}_{2D} \cdot \boldsymbol{\nabla} \mathbf{u}_{2D} &= -\boldsymbol{\nabla} p_{2D} + \nu \Delta \mathbf{u}_{2D} + \mathbf{f}_{2D}, \\ \partial_t \mathbf{u}_z + \mathbf{u}_{2D} \cdot \boldsymbol{\nabla} u_z &= +\nu \Delta u_z + \mathbf{f}_z, \end{aligned} \tag{2.7}$$

where $\mathbf{u}_{2D}$ stands for the horizontal components of the velocity field and u_z for the

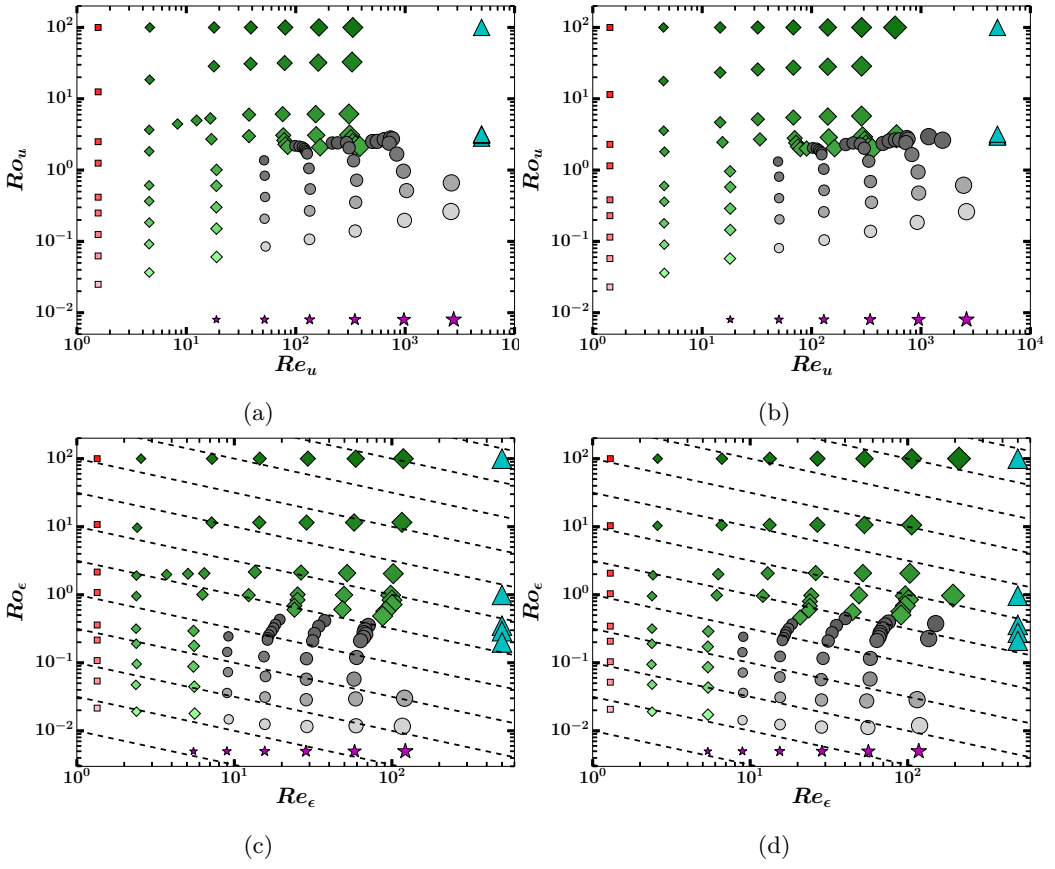

Figure 2: The figures show the location of the numerical runs in the (Ro_u, Re_u) parameter space (panels a,b) and in the $(Ro_\epsilon, Re_\epsilon)$ plane (panel c,d) for the helical flows (panels a,c) and the non-helical flow (panels b,d). Larger symbols denote larger values of Re_f and lighter symbols correspond to smaller values of Ro_f. Different symbols correspond to different behaviour of the flow.

vertical. All fields are independent of the vertical coordinate z. The points for the 2D simulations ($Ro_f = 0$ limit) are placed at the position $Ro_f = 10^{-2}$. Finally the triangles ▲ denote hyper-viscous runs obtained when we replace the Laplacian in the equation 1 with the Δ^4. Hyper-viscous runs model the limit $Re_f \to \infty$ and are place in figure 1 at the value $Re_f = 1000$.

The vertical dashed line stands for the linear stability boundary of the laminar flow. For the chosen forcing the first unstable mode is z-independent and follows the linearized version of eq. (2.7). Accordingly the unstable mode is independent of rotation and the vertical component of the laminar flow. As a result the laminar stability boundary is independent of Ro_f and is the same for the helical and the non-helical flow, that share the same laminar $\mathbf{u}_{2D}$ at $Re_f \simeq 1.278$.

Figure 2 shows the same points in the parameter plane (Re_u, Ro_u) (top panels) and $(Re_\epsilon, Ro_\epsilon)$ (bottom panels). The dashed lines in figures 2c,2d indicate values of constant Ro_λ. For the range of examined parameters, compared to the points in the (Re_f, Ro_f) plane there is a clear shift of the points to larger values of Re_u as Ro_u is decreased in

figures 2a and 2c while there is a decrease of Re_ϵ as Ro_ϵ is decreased in figures 2b and 2d.

Our principle goal in this work is using this large number of numerical simulations to determine the dependence of the large scale quantities of rotating turbulence like the saturation amplitude U and the energy dissipation rate and map the different behaviours observed in the parameter space making a phase space diagram.

3. Inverse transfers and saturation of condensates.

In this section we present some theoretical estimates for the saturation amplitude of the velocity U and the energy dissipation rate ϵ. As a first step we consider a fixed energy injection rate ϵ and use $(Re_\epsilon, Ro_\epsilon)$ as control parameters. We relax this assumption later in the text where we extend these considerations to the case of fixed forcing amplitude.

For weak rotating and non-rotating systems ($Ro \to \infty$) the cascade is strictly forward. The external forcing is balanced either by the viscous forces when Re is small, or by the nonlinearities that transfer the injected energy to the small scales where viscosity is again effective. These considerations lead to the classical scaling for laminar and turbulent flows between the velocity U and the energy injection rate ϵ,

$$U^2 \propto \epsilon \frac{\ell_f^2}{\nu} \quad \text{for} \quad Re_\epsilon \to 0 \quad \text{and} \quad U^2 \propto (\epsilon \ell_f)^{2/3} \quad \text{for} \quad Re_\epsilon \to \infty. \tag{3.1}$$

Note that both of these scalings are independent of the domain size L and the rotation rate Ω. Using these scalings one can show that for $Re_\epsilon \to \infty$ all the definitions of Re given in the previous section are equivalent up to a pre-factor so that $Re_\epsilon \sim Re_u \sim Re_f$ and $Ro_\epsilon \sim Ro_u \sim Ro_f$.

In the presence of an inverse cascade however the involved mechanisms for saturation become considerably different, altering these scaling relations. At late times, in order for the system to reach a steady state and saturate the initial increase of the large scale energy, it has to either suppress the rate that energy cascades inversely ϵ_{inv} or to reach sufficiently high amplitudes so that the energy can be dissipated by viscosity. If indeed the transition from forward to an inverse cascade has a critical behaviour, the amplitude of the inverse cascade will depend as a power law on the deviation from criticality Ro_ϵ^*,

$$\epsilon_{inv} = C_1 \left(\frac{Ro_\epsilon^* - Ro_\epsilon}{Ro_\epsilon^*} \right)^\gamma \epsilon \qquad \text{for} \quad 0 < Ro_\epsilon^* - Ro_\epsilon \ll Ro_\epsilon^*, \tag{3.2}$$

while away from criticality it is expected that,

$$\epsilon_{inv} = C_2\, \epsilon \qquad \text{for} \quad 0 < Ro_\epsilon \ll Ro_\epsilon^*. \tag{3.3}$$

Here Ro_ϵ^* denotes the critical value of Rossby for which the inverse cascade starts. Note that Ro_ϵ^* is found to depend on the height of the box but not on the horizontal dimensions. A sketch of the dependence of ϵ_{inv} on Ro_ϵ is shown at the left panel of figure 3.

The pre-factors C_1 and $C_2 \leqslant 1$ and the exponent γ have not yet been determined neither by DNS nor by experiments. In fact, even the conjecture of criticality is very hard to verify with DNS. Although it seems to be plausible, it has been demonstrated with some accuracy only for two dimensional models (see Benavides & Alexakis (2017); Seshasayanan *et al.* (2014); Seshasayanan & Alexakis (2016)). The reason is that close to the transition point, finite size and finite Reynolds effects become important that tend to smooth out the transition. To demonstrate this criticality, ever increasing box sizes and Reynolds numbers need to be considered and this is extremely costly for three dimensional simulations. We thus do expect that the transition might not appear as sharp

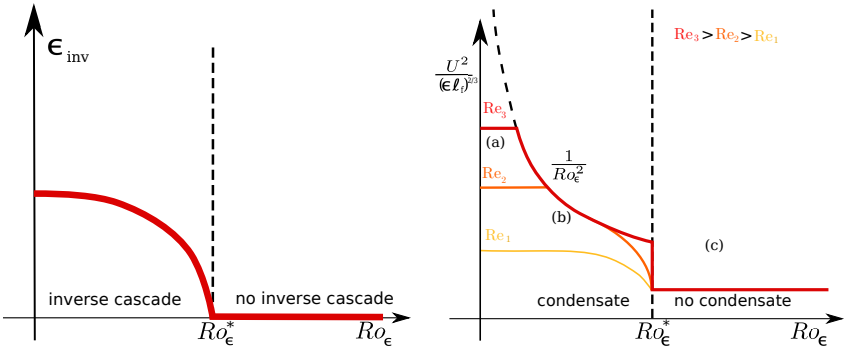

Figure 3: Left panel: The figure shows an illustration of the expected dependence of the amplitude of the inverse flux ϵ_{inv} at the early stages of the inverse cascade as a function of the Rossby number Ro_ϵ. Right panel: Figure shows an illustration of the total energy U^2 as a function of Ro_ϵ at the steady state regime for different values of Re_ϵ. The dashed vertical line indicates the transition from a flow with no inverse cascade to a flow with an inverse cascade. The dashed curved line shows the scaling $1/Ro_\epsilon^2$ that reflects the $U^2 \propto \Omega^2 L^2$ scaling.

as eq. (3.2) might suggest and we will be rather dominated by finite size effects that will smooth the transition.

For $Ro_\epsilon < Ro_\epsilon^*$ the energy that arrives at the domain size piles up forming condensates. In rotating turbulence such condensates can saturate by two possible mechanisms. First, just like in the case of 2D turbulence, saturation comes from viscous forces: the amplitude of the large scale condensate U_{2D} becomes so big that viscous dissipation at large scale balances the rate ϵ_{inv} that energy arrives at the large scales by the inverse cascade. Thus the balance $\epsilon_{inv} \propto \nu \frac{U_{2D}^2}{L^2}$ is reached. The scaling for the amplitude of the condensate close to the transition point Ro_ϵ^* thus follows,

$$U^2 \propto C_1 \frac{\epsilon L^2}{\nu} \left(\frac{Ro_\epsilon^* - Ro_\epsilon}{Ro_\epsilon^*} \right)^\gamma, \qquad \text{for} \quad 0 < Ro_\epsilon^* - Ro_\epsilon \ll Ro_\epsilon^*. \tag{3.4}$$

This argument indicates that if the injection rate ϵ is fixed, the amplitude of the condensate U scales super-critically with Ω with an exponent $\gamma/2$. For strong rotations away from criticality $Ro_\epsilon \ll Ro_\epsilon^*$, we expect the scaling for the condensate of 2D turbulence,

$$U^2 \propto C_2 \frac{\epsilon L^2}{\nu}, \qquad \text{for} \quad 0 < Ro_\epsilon \ll Ro_\epsilon^*. \tag{3.5}$$

We will refer to the condensate in this case as a *viscous condensate* because it is the viscosity that saturates the growth of energy at the large scales.

A different way to saturate the inverse cascade for fast rotating flows is by breaking the conditions that make the flow quasi-2D. This can happen in domains with periodic boundary conditions where due to the conservation of vorticity flux the shape of the condensate takes the form of a dipole with one co-rotating vortex and a counter rotating vortex. Saturation of the inverse transfer of energy can then happen when the counter rotating vortex cancels locally the rotation rate and energy cascades forward again (see Bartello *et al.* (1994); Alexakis (2015)). This balance is achieved when eddy turn over time of the condensate L/U becomes comparable to the rotation Ω. This leads to the

scaling,

$$U^2 \propto \Omega^2 L^2. \tag{3.6}$$

This scaling was realized in simulations of rotating Taylor-Green flows, see Alexakis (2015). Note that this scaling is independent of the amplitude of the inverse cascade, and thus independent from the deviation from criticality, that suggest that the transition will be sub-critical. This was indeed found to be the case in Alexakis (2015). Further more, recently Yokoyama & Takaoka (2017) were able to follow the hysteresis diagram of the subcritical bifurcation. Finally we also note that in this regime a strong asymmetry between co-rotating and counter rotating vortexes is expected, (see for example Hopfinger *et al.* (1982); Bartello *et al.* (1994); Morize & Moisy (2006); Bourouiba & Bartello (2007); Sreenivasan & Davidson (2008); Van Bokhoven *et al.* (2008); Staplehurst *et al.* (2008); Moisy *et al.* (2011); Gallet *et al.* (2014)). We will refer to the condensate in this case as a *rotating condensate* because the energy at the large scales depends on the rotation rate.

From the two mechanisms the one that predicts a smaller value of U_{2D}^2 is going to be more effective. As the Rossby number Ro_ϵ is varied slightly below the critical value, we expect that due to the small amplitude of the inverse cascade, viscosity will be effective in saturating the inverse cascade and the saturation amplitude will be given by eq. (3.4). Away from criticality however, the breaking of the quasi-2D condition becomes more effective as the amplitude predicted by (3.6) will become smaller that (3.4), and the saturation amplitude will depend on rotation as in eq. (3.6). The region for which the first scaling (3.4) holds becomes smaller as Re_ϵ increases. Thus in the limit of large Re_ϵ the transition will become discontinuous. Viscosity will become effective again at very small Ro_ϵ where the saturation amplitude will be governed by equation (3.5). The value of Ro_ϵ at which the behaviour transitions from the scaling (3.6) to the scaling (3.5) can be obtained by equating the two predictions. This leads to

$$Ro_\epsilon \propto Re_\epsilon^{-1/2} \tag{3.7}$$

which implies that the transition from a rotating condensate to a viscous condensate occurs when the micro-Rossby number is of order unity $Ro_\lambda = \mathcal{O}(1)$.

The right panel of figure 3 shows a sketch of these expected transitions. The parameter space is thus split in three regions (a) one where a condensate forms that is balanced by viscosity for $Ro_\epsilon \ll Re_\epsilon^{-1/2} \ll Ro_\epsilon^*$, (b) a second in which the condensate that forms equilibrates to a steady state by the counter rotating vortex cascading energy back to the small scales for $Re_\epsilon^{-1/2} \ll Ro_\epsilon < Ro_\epsilon^*$, and finally (c) where there is no inverse cascade and the system is close to isotropy for $Ro_\epsilon > Ro_\epsilon^*$. We stress that based on these arguments the behaviour of the flow at large Re_ϵ and low Ro_ϵ depends on precise order in which the limits $Ro_\epsilon \to 0$ and $Re_\epsilon \to \infty$ are taken.

We now relax the assumption of fixed energy injection rate and consider the case that the system is forced by a constant in time forcing of fixed amplitude as in our simulations. For weak rotation the relation between the forcing amplitude and energy injection rate if the Reynolds number is small is given by:

$$\epsilon \propto \frac{f_0^2 \ell_f^2}{\nu} \quad \text{for } Re_f \ll 1, \quad \text{(laminar scaling)}, \tag{3.8}$$

while for large Reynolds numbers we have a viscosity independent scaling:

$$\epsilon \propto f_0^{3/2} \ell_f^{1/2} \quad \text{for } Re_f \gg 1, \quad \text{(turbulent scaling)}. \tag{3.9}$$

For high rotation rates however the injection rate can depend on Ω if the forcing is not invariant along the axis of rotation. This was shown for the Taylor-Green forcing where

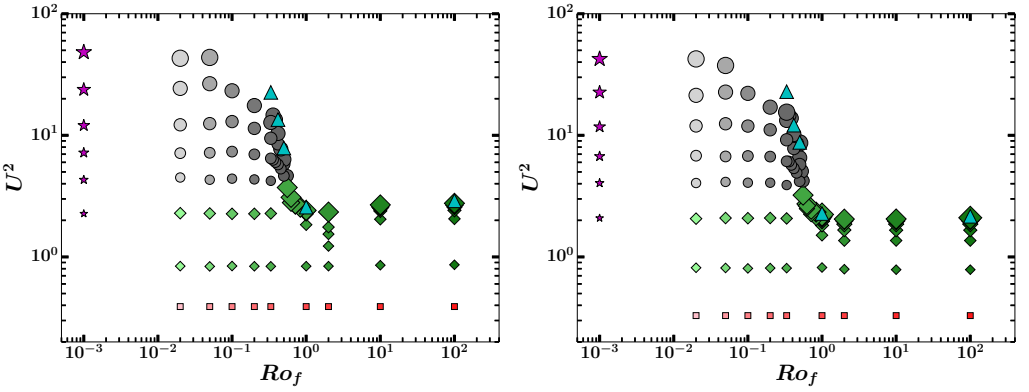

Figure 4: The figures show the total energy U^2 (in units of U_f^2) as a function of Ro_f for the examined numerical runs for a) helical flow and b) non-helical flow. Larger symbols denote larger values of Re_f and lighter symbols correspond to smaller values of Ro_f. Different symbols correspond to different behaviour of the flow.

the flow was shown to re-laminarize at high rotation rates (Alexakis 2015). This effect will not take place in the present investigation for which the forcing is z independent and we thus expect that the scaling in eq. (3.9) remains valid, that along with eq.(3.5) leads to the prediction,

$$U^2 \propto U_f^2 Re_f (k_f L)^2 \quad \text{for } Ro_f \ll 1, \tag{3.10}$$

for the amplitude of the condensate. We note that in the presence of of large scale separation this relation is altered to the weaker scaling $U^2 \propto U_f^2 Re_f^{2/3} (k_f L)^{4/3}$ due to the effect of sweeping (see Shats *et al.* (2007); Xia *et al.* (2008); Tsang & Young (2009); Gallet & Young (2013)). Such an effect however is not expected to be present in our case for which $k_f L = 4$. For moderate values of Ro_f such that the saturation comes from the cancelling of the quasi-2D condition of the counter rotating vortex, U^2 is independent of the energy injection rate and thus from the forcing amplitude. and it is thus given by eq. (3.6). Thus, a qualitative difference between the constant injection of energy and constant forcing amplitude is only expected for viscous condensates and only alters the dependence of the saturation amplitude on Re_f and not on Ro_f.

4. Simulation Results

We begin by plotting in figure 4 the square of the velocity saturation amplitude U^2 (in units of U_f^2) as a function of the Rossby number for the entirety of our data points for the helical (left panel) and the non-helical (right panel) runs. For both cases the velocity amplitude increases rapidly as Ro_f decreases beyond a critical value $Ro_f^* = \mathcal{O}(1)$. This increase appears to become stronger for larger values of Re_f (larger symbols). For larger values of Ro_f (weakly rotating runs), U_f^2 quickly saturates to a Ro_f and Re_f independent value provided Re_f is sufficiently above the laminar instability threshold.

The large increase of U^2 indicates the formation of a condensate at large scales. This is clear for large Re_f and strong rotation where Ro_f is much smaller than the critical value. However for values of the rotation close to the critical value Ro_f^* or for small Re_f for which the condensate does not obtain such large values, a better indicator for a

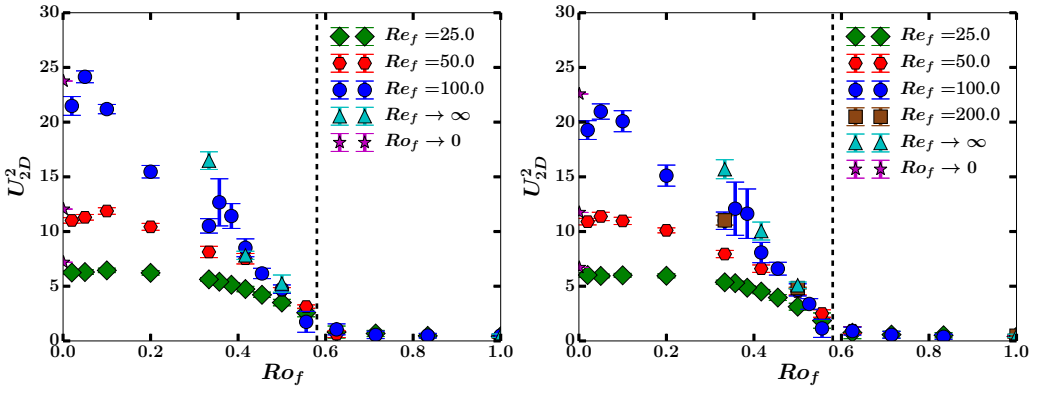

Figure 5: The figures show the energy at large scales U_{2D}^2 as a function of Ro_f (in units of U_f^2) for a few different values of Re_f for a) the helical flow and b) the nonhelical flow. The vertical dashed line at $Ro_f \sim 0.6$ denotes the critical Rossby number Ro_f^* at which the system transitions to a condensate.

condensate formation is the energy U_{2D}^2 contained in the largest Fourier mode $|\mathbf{k}| = 1$, or in terms of the energy spectrum E_k we have $U_{2D}^2 = E_1$ where

$$E_k = \left\langle \int |\hat{\mathbf{u}}(\mathbf{q})|^2 \delta(|\mathbf{q}| - k) dq^3 \right\rangle \quad \text{with} \quad \hat{\mathbf{u}}(\mathbf{q}) \equiv \frac{1}{2\pi^{3/2}} \int \mathbf{u} e^{i\mathbf{q}\cdot\mathbf{x}} dx^3 \tag{4.1}$$

Figure 5 shows U_{2D}^2 as a function of Ro_f for few different values of Re_f for the helical and the nonhelical flow. From this figure the critical value Ro_f^* is estimated to be $Ro_f^* \simeq 0.6$ for both flows. The value of Ro_f^* is denoted by a vertical dashed line in the figures. For values above Ro_f^* the large scale energy remains close to zero. Below Ro_f^* the energy U_{2D}^2 increases as Ro_f decreases further from Ro_f^* and asymptotes to a finite value as $Ro_f \to 0$ is approached.

Close to the onset the transition to the condensate appears to be supercritical, and U_{2D}^2 can be fitted to a function of the form $U_{2D}^2 \propto C_3(Ro_f^* - Ro_f)^\gamma$. From the present data we cannot measure with any significant accuracy the exponent γ. We note that increasing Re_f increases the saturation amplitude of U_{2D}^2 indicating that the prefactor C_3 depends on the Reynolds number. But in the large Re_f limit, we see that the data points converge for Ro_f close to Ro_f^*. This shows that unlike the discussion in the section 3, and the results of Alexakis (2015); Yokoyama & Takaoka (2017) the transition at large Re_f is supercritical.

For intermediate values of Ro_f and for sufficiently large values of Re_f, we are expecting that U_{2D}^2 will saturate to values that follow the scaling of the rotating condensates $U_{2D} \propto \Omega L$ (eq. (3.6)), that implies that the saturation amplitude is such that $U_{2D} Ro_f \simeq 1$. To test this expectation we plot in figure 6, $U_{2D} Ro_f$ as a function of Ro_f for different values of Re_f. Indeed in the region $0.3 > Ro_f > Ro_f^*$ the $U_{2D} Ro_f$ appears to converge to an order one value as Re_f is increased, independent of Ro_f. We note that the largest Re_f points are close to the hyper viscous results and this implies independence on Re_f has been reached. Although the results indicate that the saturation mechanism leading to eq. (3.6) is plausible, the range of validity is very small to claim that the scaling has been demonstrated. To extend the range of validity to smaller values of Ro_f we need to extend our simulations to larger values of Re_f. This however becomes numerically very costly not

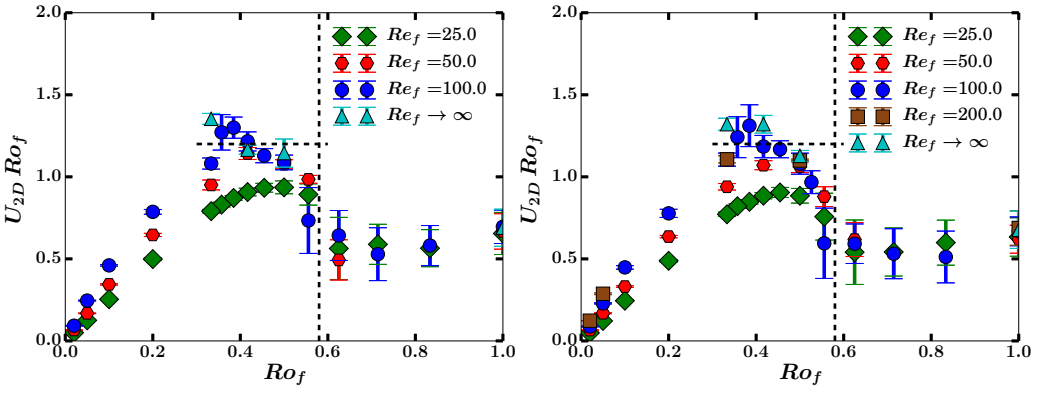

(a) (b)

Figure 6: The figures show the product $U_{2D}\,Ro_f$ (in units of U_f) as a function of Ro_f for a few different values of Re_f for a) the case of helical flow and b) the case of the nonhelical flow. The vertical dashed line at $Ro_f \sim 0.6$ denotes the critical Rossby number for the transition to condensates. The horizontal dashed line denotes the scaling $U_{2D}\,Ro_f \sim 1$.

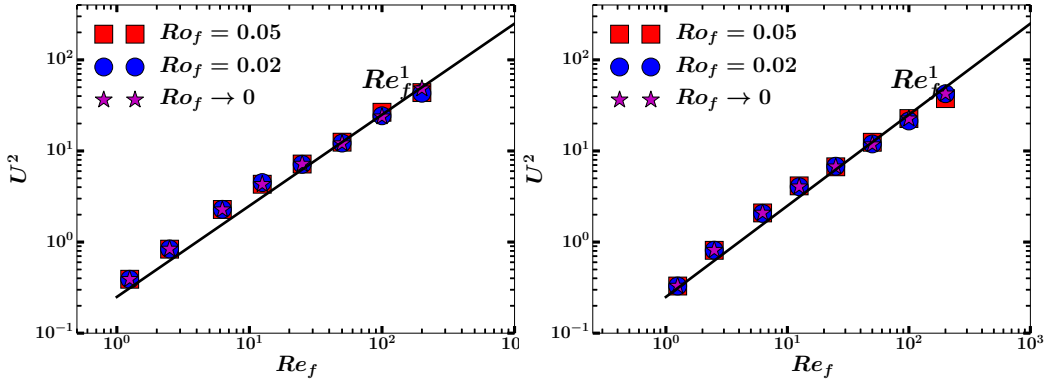

(a) (b)

Figure 7: The figures show the energy U^2 (in units of U_f^2) as a function of Re_f for a few different values of $Ro_f \ll 1$ for a) the case of helical flow and b) the case of the nonhelical flow. The thick line denotes the linear scaling with Re_f.

only because it implies an increase of resolution but also because the saturation amplitude of the condensate becomes large, and the time-scale to reach saturation increases. As an example we mention that if we would like to extend the range of the rotating condensate to a value of Ro_ϵ twice smaller, it will require to achieve a Re_ϵ that it is four times as big as the one used now. This would require a spatial grid that is $4^{3/4}$ bigger in each direction. If we take in to account the computational cost increase due to the CFL condition (Courant *et al.* 1928) by a factor of $2 \times 4^{3/4}$ (due to the finer grid and twice larger U) and the twice longer duration of the run we arrive at a computational cost that is 2^8 more expensive than the present computations.

Finally in figure 5, for very small values of Ro_f the energy U_{2D}^2 asymptotes to a finite value. This value matches the results obtained from the $2D$ simulations using equation (2.7) that are marked by a star, indicating that the flow has become two dimensional.

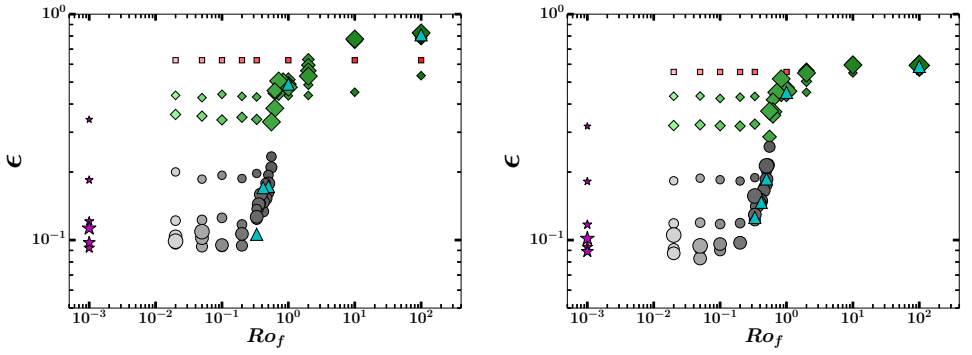

Figure 8: The figures show the injection/dissipation rate ϵ (in units of $U_f^3 k_f$) as a function of Ro_f for the examined numerical runs for a) the helical flow and b) the nonhelical flow. Larger symbols denote larger values of Re_f and lighter symbols correspond to smaller values of Ro_f. Different symbols correspond to different behaviour of the flow.

The saturation amplitude U_{2D}^2 at the $Ro_f = 0$ limit however depends on the value of Re. In figure 7 we plot U^2 for the smallest values of Ro_f examined as a function of Re_f along with the results from the system (2.7). The data scale linearly with Re_f in agreement with the prediction given in eq. (3.10) for the viscous condensate. Equating the two results shown in figure 6 and in figure 7 we obtain that the transition from the rotating condensate regime to the viscous condensate regime occurs when $Ro_f^{-2} \sim Re_f$ as seen in eq. (3.7).

We now focus on the effect of rotation on the energy injection rate in the system. In figure 8 we plot the energy injection rate ϵ (in units of $f_0^{3/2} k_f^{1/2}$) as a function of Ro_f for the entirety of our data points for the helical (left panel) and the non-helical (right panel) runs. We remind the reader that smaller symbols indicate smaller Reynolds numbers as in figure 1. The energy dissipation as Re_f increases (from small to large symbols), saturates to a Re_f independent value. This value however is different for small and large values of Ro_f with the transition occurring over a thin region close to $Ro_f = Ro_f^*$. This is seen more clearly in figure 9 where we have concentrated to five largest values of Re_f and plotted the data in linear scale close to Ro_f^*. For these values of Re_f, the energy injection rate is decreased to a five times smaller value as Ro_f is decreased. The transition from one value to the other occurs very fast when Ro_f is close to its critical value $Ro_f^* = 0.6$. The transition by this sudden jump at Ro_f^* indicates that possibly close to the critical point the dependence of ϵ on Ro_f could be discontinuous or an other possibility is that it is continuous but with diverging derivatives. Similar behaviour has been observed close to the transition to an inverse cascade for a 2DMHD flow where the low dimensionality of the system allowed a much closer investigation. In any case the investigation of the energy injection close to critical rotation rate is very interesting but would require long runs that are expensive for numerical simulations but could be addressed more easily with experiments.

We conclude this section by considering the ratio $\epsilon/(U^3 k_f)$. The quantity $\epsilon/(U^3 k_f)$ is sometimes referred as the drag coefficient. For laminar flows it scales like $1/Re_u$ while it tends to a non-zero constant for strongly turbulent flows at large Re_u. The finite asymptotic value of this ratio at large Re_u gives one of the fundamental assumptions of turbulence theory, that of finite dissipation at the zero viscosity limit. This has been

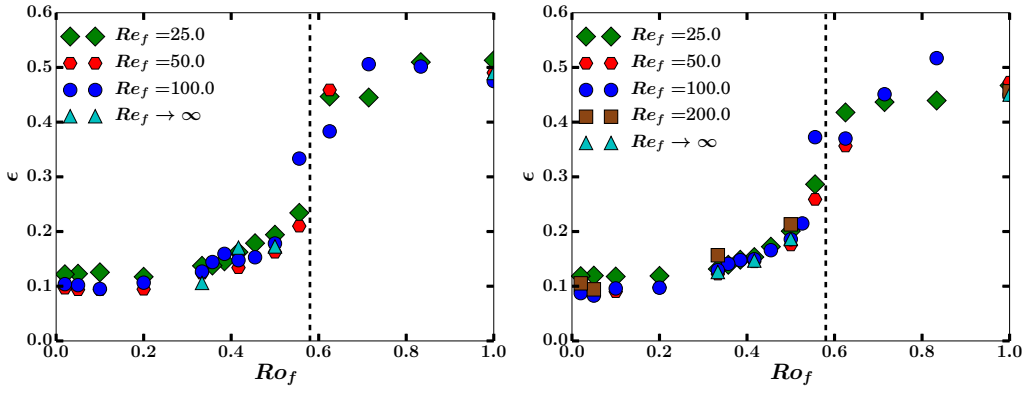

Figure 9: The figures show the dissipation rate ϵ (in units of $U_f^3 k_f$) as a function of Ro_f for a few different values of Re_f for a) the case of helical flow and b) the case of the nonhelical flow. The vertical dashed line at $Ro_f \sim 0.6$ denotes the critical Rossby number for the transition to condensates.

clearly demonstrated in experiments of non rotating turbulence and large scale numerical simulations, see Sreenivasan (1984); Kaneda *et al.* (2003); Ishihara *et al.* (2016). In rotating turbulence experiments it has been investigated in Campagne *et al.* (2016), where the drag coefficient has been shown to scale as Ro_u for sufficiently small Ro_u. We note that in their experimental set-up it was the velocity of the propellers that were used to define Ro_u. In figure 10 we plot the ratio $\epsilon/(U^3 k_f)$ as a function of Re_u for different Rossby numbers. The arrow indicates the direction that Ro_f is increased (ie rotation is decreased). The dashed lines connect points with the same value of Ro_f for three different values of $Ro_f = 1.0, 0.5, 0.33$ as we move from top to bottom.

For rotation rates such that $Ro_f > Ro_f^*$ (diamonds), the data show a Re_u^{-1} scaling at low Re_u that transitions to a constant at large Re_u demonstrating a finite dissipation at infinite Re_u. This asymptotic value decreases slightly with Ro_f. For the runs with $Ro_f < Ro_f^*$ (circles) on the other hand, the region of the laminar scaling Re_u^{-1} appears to extend to larger values of Re_u. The very fast rotating runs (circles with light colours) and the $2D$ simulations from eq. (2.7) show a Re_u^{-1} scaling through out the examined range. The pre-factor in front of Re_u^{-1} has decreased at the condensate regime because the laminar vortices are at the scale of the forcing (eq. (3.1)) while the viscous condensate vortices are at the scale of the box size eq. (3.5). However, for fixed Ro_f (dashed lines), as the Reynolds number is increased the Re_u^{-1} scaling appears to flatten to a Re_u independent scaling. This occurs for the flows that are in the rotating condensate regime. This suggests that even for the rotating runs, the ratio $\epsilon/(U^3 k_f)$ will reach an asymptotic non-zero value at $Re_u \to \infty$ (for fixed Ro_f) matching the one obtained by the hyper-viscous simulations. This asymptotic value however is different for different values of Ro_f. Indicating that the value of the drag coefficient depends on the Rossby number.

The values of this asymptotic behaviour along with the results of the hyper viscous runs are shown in figure 11 where they are compared with the scaling $\epsilon/(U^3 k_f) \propto Ro_f^3$ that is the scaling obtained if assuming the saturation amplitude follows $U \propto \Omega L$. The data appear to be slightly steeper. Perhaps this is not surprising considering the small range of Ro_f that the scaling $U \propto \Omega L$ was shown to hold in figure 6. Note that a weak turbulence scaling would predict $\epsilon/(U^3 k_f) \propto Ro_\epsilon$ that is clearly not obtained here.

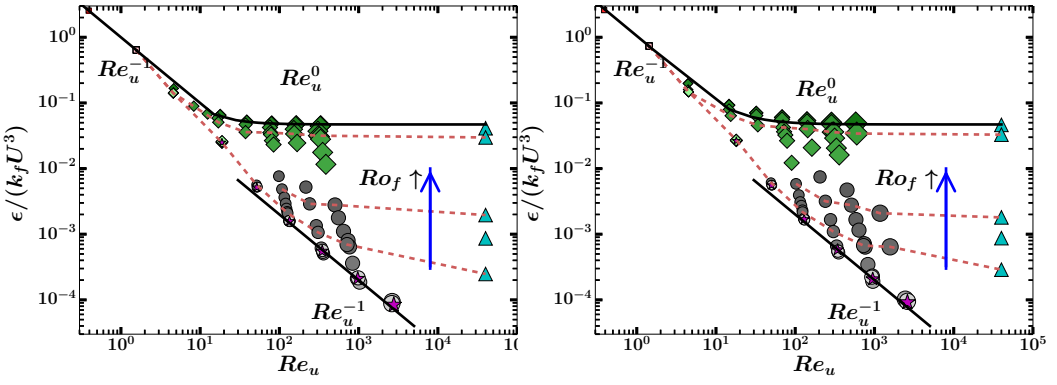

(a) (b)

Figure 10: The figures show the normalized dissipation rate $\epsilon/(U^3 k_f)$ as a function of Re_u for the examined numerical runs for a) the helical case and b) the nonhelical case. Larger symbols denote larger values of Re_f and lighter symbols correspond to smaller values of Ro_f. Different symbols correspond to different behaviour of the flow. The thick lines denote the laminar scaling Re_u^{-1} and the turbulent scaling Re_u^0. The blue vertical arrow indicates the direction of increasing Ro_f (decreasing Ω). The three dashed brown lines connect the data points of three values $Ro_f = 1.0, 0.5, 0.33$ as we move from top to bottom.

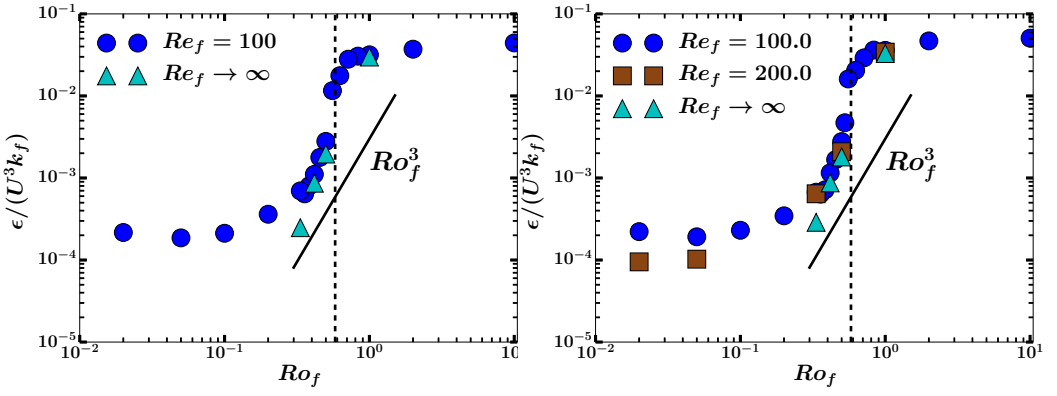

(a) (b)

Figure 11: The figures show the normalized dissipation rate $\epsilon/(U^3 k_f)$ as a function of Ro_f for a few different values of $Re_f \gg 1$ for a) the case of helical flow and b) the case of the nonhelical flow. The thick line denotes the scaling Ro_f^3 and the vertical dashed line denotes the critical Rossby number for the transition to condensates.

5. Structures, Spectra and Dynamical behaviour

In this section we try to obtain an understanding of the results in the previous section by visualizing the structures involved and examining their spectral and temporal behaviour. We start by the visualization of the flows. Figure 12 shows colour coded visualizations of the vertical vorticity field. The red colour corresponds to vorticity parallel to rotation while the blue colours correspond to vorticity anti parallel to rotation. The three images have been constructed from numerical simulations corresponding to

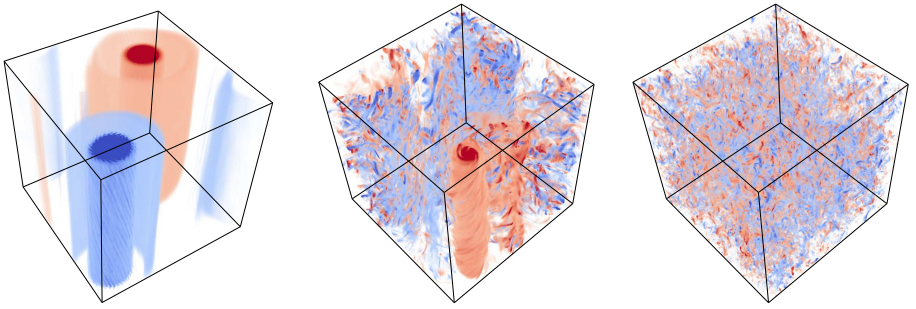

(a) (b) (c)

Figure 12: The figures show the contours of the vertical vorticity ω_z for a) $Ro_f = 0.02, Re_f = 100$, b) $Ro_f = 0.5, Re_f = 100$, c) $Ro_f = \infty, Re_f = 100$. The red colour corresponds to positive vorticity and the blue colour corresponds to negative vorticity.

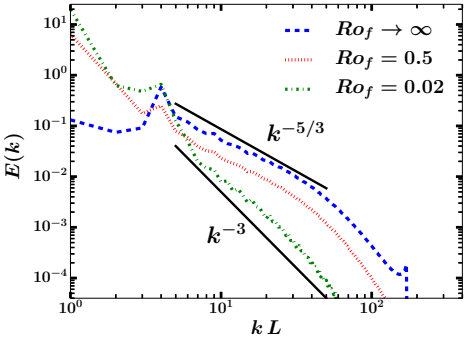

Figure 13: The figure show the energy spectra for a few different values of Ro_f with $Re_f = 100$. The black thick lines denote the scaling $k^{-5/3}, k^{-3}$.

the three regimes discussed in the previous section, (a) the viscous condensate, (b) the rotating condensate with the counter rotating vortex cascading energy back to the small scales and (c) weakly rotating (or non-rotating) turbulence. In the first case (a) the flow looks very close to a 2D state with no visible variations along the z direction and no observed asymmetry between co-rotating and counter-rotating vortex. In the second case (b) a condensate is also formed but only clearly observed for the co-rotating vortex. The counter rotating vortex, although present, is infested with small scale eddies that extract energy from it. Finally in case (c) no large scale condensate is observed and the flow looks isotropic.

The spectra for the three cases are shown in the figure 13. The spectrum for the flow in the viscous condensate regime (a) is shown with a green dash dot line. The energy is concentrated at the smallest wavenumber $kL = 1$, with the energy for wave numbers above $k_f L = 4$ dropping very fast. In the non rotating case (c), shown by a dashed line, energy is concentrated at the forcing wavenumber $k_f L = 4$ that is followed by a power-law spectrum close to $k^{-5/3}$. Finally, the case in the intermediate regime (b) shown by the dotted line, shows signs of both behaviours: the energy is concentrated at the largest scale $kL = 1$ as in case (a) but the spectrum at the small scales follows a $k^{-5/3}$ power-law as in the non-rotating case. Thus the spectrum for the rotating condensate is in agreement with the co-existence of a condensate along with a forward cascade.

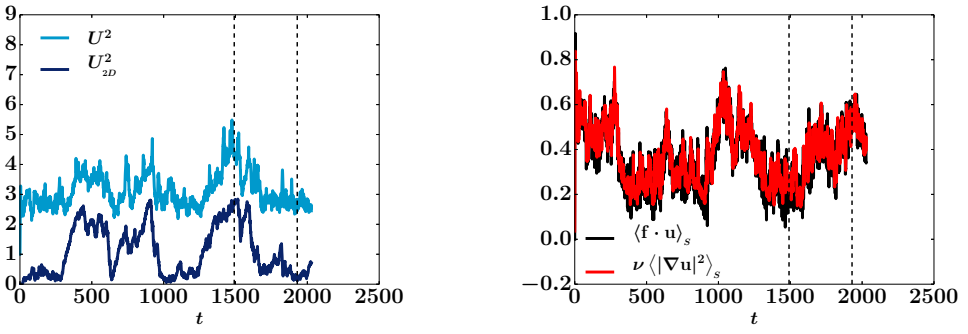

(a) (b)

Figure 14: The figure a) show the time series of the total energy U^2 and the energy at the large scales U^2_{2D} for the case of $Ro_f = 0.556, Re_f = 100$ which is close to Ro^*_f. The vertical dashed lines denote the time instances at which the visualizations 15 are taken. Figure b) shows the spatial averaged energy injection rate $\langle \mathbf{f} \cdot \mathbf{u} \rangle_S$ and the dissipation rate $\nu \langle |\boldsymbol{\nabla} \mathbf{u}|^2 \rangle_S$ for the same run.

We next examine the behaviour of the flow close to the transition point Ro^*_f. The arguments made in section 3 suggested that at large Re_f this transition would become discontinuous (subcritical) which was what was found for the Taylor-Green forcing Alexakis (2015); Yokoyama & Takaoka (2017). The results in the previous section however showed that even at large Re_f the transition remains supercritical.

To understand this discrepancy, in figure 14a we show the time evolution of the total energy U^2 with a dark line and the energy of the large scales U^2_{2D} for a value of $Ro_f = 0.556$ close to the critical value and a relative large $Re_f = 100$. The flow randomly oscillates between two distinct states: one where the energy of the large scales is weak and most of the energy lies in the forcing scales and one where the energy of the large scales dominates and accounts for more than 60% of the total energy. The energy at the large scales varies by an order of magnitude between these two states with $U^2_{2D} \sim \Omega L$ when U^2_{2D} dominates and $U^2_{2D} \ll \Omega L$ at its low values. In the panel 14b the time series of the spatial averaged energy injection rate $\langle \mathbf{f} \cdot \mathbf{u} \rangle_S$ and the energy dissipation rate $\nu \langle |\boldsymbol{\nabla} \mathbf{u}|^2 \rangle_S$ is shown. A burst of energy dissipation is observed at the time instances that the flow transitions from the condensate to the 3D turbulent state. This correlation between the change of state in the large scales and the energy dissipation/injection is typical of bimodal systems (Mishra *et al.* 2015). Visualizations of the vertical vorticity of the flow are shown in figure 15 at the two different times indicated by the vertical dashed lines in figure 14a and 14b. The two figures resemble the ones shown in panel (b) and (c) in figure 12 that were obtained for different values of the parameter Ro_f.

It appears thus that the transition from isotropic turbulence to rotating condensate occurs through a bistable regime where both states are realized at different instances of time. The two state are distinct i.e. they are separated by finite amount of energy however the time the system spends in each one of these states can depend on the deviation from the onset Ro^*_f, becoming infinite for the condensate state for Ro_f sufficiently smaller than Ro^*_f. The time averaged quantities displayed in the previous sections thus remain continuous. This bistable behaviour if it persists at larger Re_f will indicate that the transition will remain supercritical. Similar behaviour has been observed in experiments in a rotating tank where intermittent switching between blocked and large scale zonal

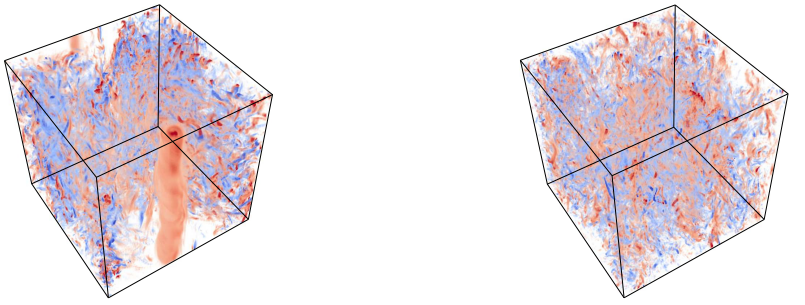

(a) (b)

Figure 15: The figures show the contours of the vertical vorticity ω_z for $Ro_f = 0.556, Re_f = 100$ for the two time instances marked in figure 14a. The red colour corresponds to positive vorticity and the blue colour corresponds to negative vorticity. The figure a) shows a co-rotating vortex formed when the system is in the condensate regime, while the figure b) does not have any large scale structure.

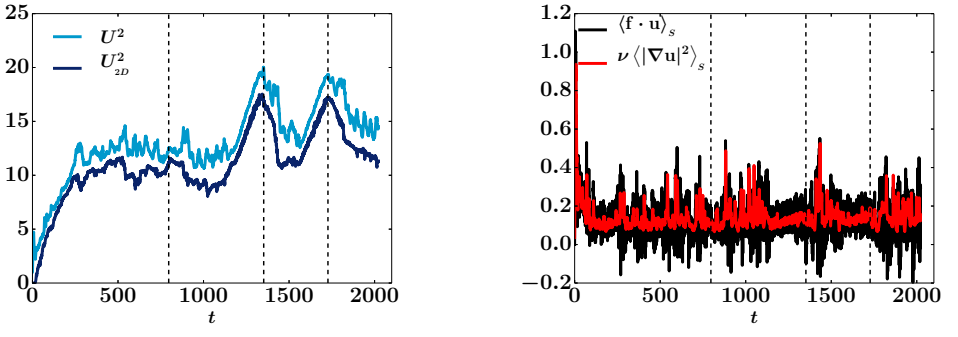

(a) (b)

Figure 16: The figure a) show the time series of the total energy U^2 and the energy at the large scales U^2_{2D} for the case of $Ro_f = 0.357, Re_f = 100$ which is close to Ro^*_f. The vertical dashed lines denote the time instances at which the visualizations 17 are taken. Figure b) shows the spatial averaged energy injection rate $\langle \mathbf{f} \cdot \mathbf{u} \rangle_S$ and the dissipation rate $\nu \langle |\nabla \mathbf{u}|^2 \rangle_S$ for the same run.

patterns have been observed Weeks *et al.* (1997). This presents an alternate mechanism other than the sub-critical transition discussed in 3 and observed in Alexakis (2015); Yokoyama & Takaoka (2017).

A similar oscillating behaviour is observed even further from the onset Ro^*_f. In figure 16a we show the time evolution of U^2_{2D} and U^2 as in figure 14a for a slightly smaller value of $Ro_f = 0.357$. Although, the system never returns to the isotropic case and U^2_{2D} is always dominant, strong fluctuations are still present. Figure 16b shows the time series of the spatially averaged energy injection rate $\langle \mathbf{f} \cdot \mathbf{u} \rangle_S$ and the energy dissipation rate $\nu \langle |\nabla \mathbf{u}|^2 \rangle_S$ for the same run as 16a. Again peaks of energy injection/dissipation are correlated with changes in the large scale flow states. We note that in the condensate regime, even though the dissipation is always positive, the energy injection rate takes both negative and positive values. This means that at certain instances of time the forcing takes energy out of the system. Visualization of the flows in figure 17 at different times

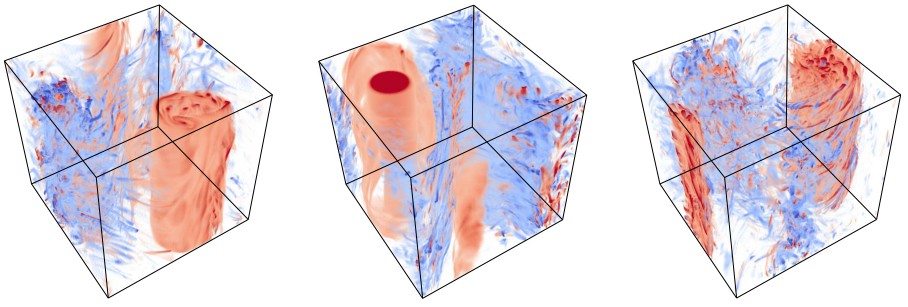

(a) (b) (c)

Figure 17: The figures show the contours of the vertical vorticity ω_z for $Ro_f = 0.357, Re_f = 100$ for the three time instances marked in figure 16a. The red colour corresponds to positive vorticity and the blue colour corresponds to negative vorticity.

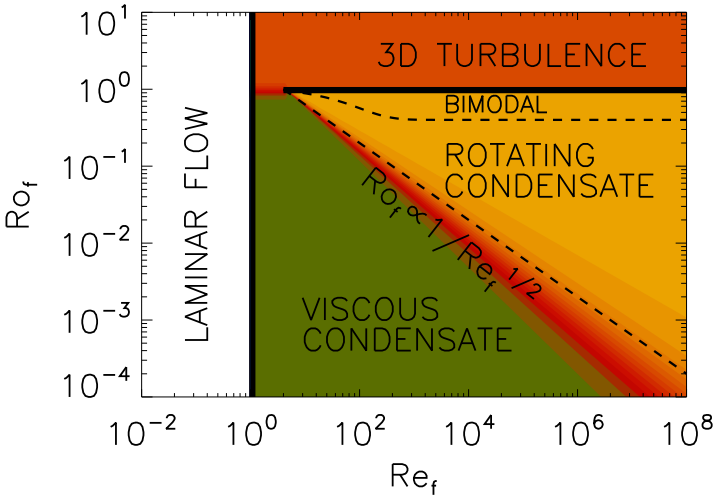

Figure 18: The figure shows the phase space diagram with the different flow behaviour marked. Solid lines denote sharp/critical transitions. Dashed line denotes smooth transitions.

reveal that these fluctuations correspond to a transition of the flow from a state that has a co-rotating vortex that is stable to states that are unstable to 3D fluctuations that however fail to destroy it. It seems thus that the key for understanding the behaviour of this flow lies in understanding the stability properties of these free evolving vortexes.

6. Conclusions

This work has given a description of steady state rotating turbulence when the forcing acts directly on the slow manifold, by mapping to the parameter space the different behaviours observed and the resulting scaling relations. Our results are concisely summarized in figure 18 where the four different phases of the rotating flows examined

are shown in the parameter space Re_f, Ro_f: Laminar flow, 3D turbulence flow, rotating condensate flow and viscous condensate flow. Solid lines indicate the boundaries where a critical transition take place, while dashed lines indicate smooth transitions.

For values of Re_f bellow a critical value Re_f^* that is independent of Ro_f the flow has a laminar behaviour. At this state the resulting flow is 2D, time independent and proportional to the inverse Laplacian of the forcing. The first unstable mode in this laminar state is a 2D mode that is not affected by the rotation and thus the instability boundary does not depend on Ro_f.

For $Re_f \gg Re_f^*$ and Ro_f above a critical value Ro_f^* the flow displays quasi isotropic 3D turbulence. This regime is described to a good degree by Kolmogorov-Richardson phenomenology Kolmogorov (1941); Richardson (1926) and classical results of turbulence like the finite energy dissipation at zero viscosity limit and a $k^{-5/3}$ energy spectrum appear to hold.

For $Re_f \gg Re_f^*$ and $Re_f^{-1/2} \ll Ro_f \leqslant Ro_f^*$ the flow is shown to be in what we refer as a rotating condensate state. In this state a co-rotating 2D vortex is dominating at the large scales while the counter rotating vortex breaks down to 3D eddies cascading energy back to the small scales. At this state the amplitude of the condensate U_{2D} (in the rather small range examined by our simulations) was shown to be proportional to the rotation rate $U_{2D} \propto \Omega L$. Our results also indicated (with the help of hyper-viscous simulations) that in this regime the finite energy dissipation at zero viscosity limit still holds but with a drag coefficient that rapidly decreases with Ro_f. The spectra at the small scales follow a close to $k^{-5/3}$ power-law, while a large peak appears at the largest scale indicating the presence of the condensate.

The transition from the quasi isotropic 3D turbulent state to the rotating condensate state was shown to be supercritical, contrary to the arguments described in the introduction that were predicting that at sufficiently large Re_f right bellow criticality Ro_f^* the system would transition discontinuously to the rotating condensate value $U_{2D}^2 \propto \Omega^2 L^2$. The reason for this discrepancy is in part because the arguments in section 3 assumed weak dependence of the energy injection rate ϵ at criticality while the DNS showed a strong sensitivity of ϵ on Ro_f close to criticality. The second reason is that the system close to criticality showed a bimodal behaviour where part of the time it was spending in the 3D turbulence state with $U_{2D}^2 \ll \Omega^2 L^2$ and remaining part was spent in the rotating condensate state with $U_{2D}^2 \propto \Omega^2 L^2$. Despite the fact that these states appeared distinct, the time spent in the condensate state can decrease continuously to zero as $Ro_f \to Ro_f^*$ (from below) leading to a continuous supercritical transition.

For $Re_f \gg Re_f^*$ and $Ro_f \ll Re_f^{-1/2}$ the flow is shown to be in what we refer to as a viscous condensate state. In this state the flow is close to 2D and both the co-rotating and counter-rotating 2D vortex exist and dominate the large scales. The flow has a normalized energy dissipation rate that decreases with Re_u following the laminar scaling Re_u^{-1}. The transition from the rotating condensate regime to the viscous condensate was found to be smooth. We note however that an other critical value of Ro_f is expected for which the flow becomes exactly 2D and all 3D perturbations decay exponentially (Gallet 2015). Such a transition is expected at even smaller values of Ro_f and to observe it we have to focus on deviations from 2D flows which was not done in the present study. A similar study in thin layers has shown that this transition is governed by strong intermittent events Benavides & Alexakis (2017). This is thus an interesting limit that is worth investigating in the future.

The difference between the parameters (Re_f, Ro_f) and (Re_u, Ro_u) or $(Re_\epsilon, Ro_\epsilon)$ was not found to be as severe as in the Taylor-Green flow where discontinuous (sub-critical)

transitions were present which resulting in mapping from one set of parameters to the other not to be one to one nor onto. In particular the difference between (Re_f, Ro_f) and $(Re_\epsilon, Ro_\epsilon)$ was only found to be significant close to the critical point Ro_f^* where ϵ was found to change abruptly. The difference between (Re_f, Ro_f) and (Re_u, Ro_u) was stronger and is due the fact that in the rotating condensate regime the scaling $U \propto \Omega L$ merged all values of Ro_u to be close to unity. This left all larger values of Ro_u to be in the viscous condensate regime. Thus, at the steady state regime at least Ro_u does not appear to be a good indicator for the strength of rotation.

We stress the importance of the ordering of the limits when one considers the low Rossby large Reynolds limits. If one considers the $Ro_f \to 0$ limit first and afterwards the $Re_f \to \infty$ one always falls in the viscous condensate regime. While if one considers the $Re_f \to \infty$ first one falls in the rotating condensate regime. To distinguish between the two one needs to look at the product $Ro_f Re_f^{1/2}$ or $Ro_\lambda = Ro_\epsilon Re_\epsilon^{1/2}$. Referring thus to the large Reynolds number, small Rossby number limit is ambiguous unless the ordering is specified.

Finally we comment on the effect of boundaries and the realizability of the present results in experiments. In the present results we considered only the simplest domain that of a triple periodic geometry and we should give word of caution in extrapolating them to domains with no slip boundary conditions. In the presence of no slip boundaries, rotation will introduce Ekman layers, Ekman (1905), that can lead to large scale drag effects (Caldwell *et al.* 1972; Howroyd & Slawson 1975; Zavala Sansón *et al.* 2001; Sous *et al.* 2013), altering in part the energy balance. Nonetheless we do believe that in a carefully prepared experimental setup where these effects are accounted for some of the presently observed phenomena would carry over to no-slip boundary conditions. In particular, it would be interesting to investigate the transition to the rotating condensate regime from 3D turbulence that displayed such rich behaviour. The high numerical cost of 3D simulations at this regime limits our runs to relatively short times and does not allow us to study in detail their statistical behaviour. Experiments in which long signals are much easier attainable can then address this issue.

The authors would like to thank various discussions with Stephan Fauve and the nonlinear physics group at ENS. This work was granted access to the HPC resources of MesoPSL financed by the Region Ile de France and the project Equip@Meso (reference ANR-10-EQPX-29-01) of the program Investissements d'Avenir supervised by the Agence Nationale pour la Recherche and the HPC resources of GENCI-TGCC-CURIE & GENCI-CINES-OCCIGEN (Project No. x2015056421 & No. x2016056421 & No. x2017056421) where the present numerical simulations have been performed.

REFERENCES

Alexakis, A. 2011 Two-dimensional behavior of three-dimensional magnetohydrodynamic flow with a strong guiding field. *Phys. Rev. E* **84** (5), 056330. 1

Alexakis, A. 2015 Rotating taylor–green flow. *J. Fluid Mech.* **769**, 46–78. 1, 2, 3, 3, 3, 4, 5, 5

Baroud, Charles N, Plapp, Brendan B, She, Zhen-Su & Swinney, Harry L 2002 Anomalous self-similarity in a turbulent rapidly rotating fluid. *Physical Review Letters* **88** (11), 114501. 1

Baroud, Charles N, Plapp, Brendan B, Swinney, Harry L & She, Zhen-Su 2003 Scaling in three-dimensional and quasi-two-dimensional rotating turbulent flows. *Physics of Fluids* **15** (8), 2091–2104. 1

Bartello, P., Metais, O. & Lesieur, M. 1994 Coherent structures in rotating three-dimensional turbulence. *J. Fluid Mech.* **273**, 1–29. 1, 3, 3

Benavides, Santiago Jose & Alexakis, Alexandros 2017 Critical transitions in thin layer turbulence. *Journal of Fluid Mechanics* **822**, 364–385. 1, 3, 6

Biferale, Luca, Bonaccorso, Fabio, Mazzitelli, Irene M, van Hinsberg, Michel AT, Lanotte, Alessandra S, Musacchio, Stefano, Perlekar, Prasad & Toschi, Federico 2016 Coherent structures and extreme events in rotating multiphase turbulent flows. *Physical Review X* **6** (4), 041036. 1

Bourouiba, Lydia & Bartello, Peter 2007 The intermediate rossby number range and two-dimensional–three-dimensional transfers in rotating decaying homogeneous turbulence. *Journal of Fluid Mechanics* **587**, 139–161. 3

Caldwell, D. R., Van Atta, C. W. & Helland, K. N. 1972 A laboratory study of the turbulent ekman layer. *Geophys. & Astrophys. Fluid Dyn.* **3** (1), 125–160. 6

Campagne, A., Gallet, B., Moisy, F. & Cortet, P.-P. 2014 Direct and inverse energy cascades in a forced rotating turbulence experiment. *Physics of Fluids* **26** (12), 125112. 1

Campagne, A., Gallet, B., Moisy, F. & Cortet, P.-P. 2015 Disentangling inertial waves from eddy turbulence in a forced rotating-turbulence experiment. *Phys. Rev. E.* **91** (4), 043016. 1

Campagne, Antoine, Machicoane, Nathanaël, Gallet, Basile, Cortet, Pierre-Philippe & Moisy, Frédéric 2016 Turbulent drag in a rotating frame. *Journal of Fluid Mechanics* **794**, R5. 1, 4

Celani, A., Musacchio, S. & Vincenzi, D. 2010 Turbulence in More than Two and Less than Three Dimensions. *Physical Review Letters* **104** (18), 184506. 1

Chen, Q., Chen, S., Eyink, G. L. & Holm, D. D. 2005 Resonant interactions in rotating homogeneous three-dimensional turbulence. *J. Fluid Mech.* **542**, 139–164. 1

Courant, R., Friedrichs, K. & Lewy, H. 1928 Über die partiellen Differenzengleichungen der mathematischen Physik. *Math. Ann.* **100**, 32–74. 4

Dallas, Vassilios & Tobias, Steven M 2016 Forcing-dependent dynamics and emergence of helicity in rotating turbulence. *Journal of Fluid Mechanics* **798**, 682–695. 1

Deusebio, E., Boffetta, G., Lindborg, E. & Musacchio, S. 2014 Dimensional transition in rotating turbulence. *Phys. Rev. E* **90** (2), 023005. 1

Dickinson, S. C. & Long, R. R. 1983 Oscillating-grid turbulence including effects of rotation. *J. Fluid Mech.* **126**, 315–333. 1

Ekman, V. W. 1905 On the influence of the earth\'s rotation on ocean currents. *Ark. Mat. Astron. Fys.* **2**, 1–53. 6

Favier, B., Godeferd, F. S. & Cambon, C. 2010 On space and time correlations of isotropic and rotating turbulence. *Phys. Fluids* **22** (1), 015101. 1

Gallet, B. 2015 Exact two-dimensionalization of rapidly rotating large-reynolds-number flows. *J. Fluid Mech.* **783**, 412–447. 1, 6

Gallet, B., Campagne, A., Cortet, P.-P. & Moisy, F. 2014 Scale-dependent cyclone-anticyclone asymmetry in a forced rotating turbulence experiment. *Physics of Fluids* **26** (3), 035108. 3

Gallet, B. & Young, W. R. 2013 A two-dimensional vortex condensate at high reynolds number. *J. Fluid Mech.* **715**, 359–388. 3

Galtier, S. 2003 Weak inertial-wave turbulence theory. *Phys. Rev. E* **68** (1), 015301. 1

Godeferd, FS & Lollini, L 1999 Direct numerical simulations of turbulence with confinement and rotation. *Journal of Fluid Mechanics* **393**, 257–308. 1

Greenspan, HP 1968 The theory of rotating fluids cambridge university press. *Cambridge, England* . 1

Hopfinger, EJ & Heijst, GJFV 1993 Vortices in rotating fluids. *Annual review of fluid mechanics* **25** (1), 241–289. 1

Hopfinger, E. J., Browand, F. K. & Gagne, Y. 1982 Turbulence and waves in a rotating tank. *J. Fluid Mech.* **125**, 505–534. 1, 3

Hough, S. S. 1897 On the Application of Harmonic Analysis to the Dynamical Theory of the Tides. Part I. On Laplace's "Oscillations of the First Species," and on the Dynamics of Ocean Currents. *Philos. Trans. R. Soc. London A* **189**, 201–257. 1

Howroyd, G.C. & Slawson, P.R. 1975 The characteristics of a laboratory produced turbulent ekman layer. *Boundary-Layer Meteorology* **8** (2), 201–219. 6

Ibbetson, A & Tritton, DJ 1975 Experiments on turbulence in a rotating fluid. *Journal of Fluid Mechanics* **68** (4), 639–672. 1

Ishihara, Takashi, Morishita, Koji, Yokokawa, Mitsuo, Uno, Atsuya & Kaneda, Yukio 2016 Energy spectrum in high-resolution direct numerical simulations of turbulence. *Physical Review Fluids* **1** (8), 082403. 4

Kaneda, Yukio, Ishihara, Takashi, Yokokawa, Mitsuo, Itakura, Kenichi & Uno, Atsuya 2003 Energy dissipation rate and energy spectrum in high resolution direct numerical simulations of turbulence in a periodic box. *Physics of Fluids* **15** (2), L21–L24. 4

Kolmogorov, A. N. 1941 The local structure of turbulence in incompressible viscous fluid for very large reynolds number. *Proceedings of the USSR Academy of Sciences* **30**, 299303. 6

Kraichnan, R. H. 1967 Inertial ranges in two-dimensional turbulence. *Tech. Rep.*. DTIC Document. 1

Machicoane, Nathanaël, Moisy, Frédéric & Cortet, Pierre-Philippe 2016 Two-dimensionalization of the flow driven by a slowly rotating impeller in a rapidly rotating fluid. *Phys. Rev. Fluids* **1**, 073701. 1

Marino, Raffaele, Mininni, Pablo Daniel, Rosenberg, Duane & Pouquet, Annick 2013 Inverse cascades in rotating stratified turbulence: Fast growth of large scales. *EPL (Europhysics Letters)* **102** (4), 44006. 1

Marino, R., Pouquet, A. & Rosenberg, D. 2015 Resolving the Paradox of Oceanic Large-Scale Balance and Small-Scale Mixing. *Physical Review Letters* **114** (11), 114504. 1

Mininni, P. D., Alexakis, A. & Pouquet, A. 2009 Scale interactions and scaling laws in rotating flows at moderate Rossby numbers and large Reynolds numbers. *Phys. Fluids* **21** (1), 015108. 1

Mininni, P. D. & Pouquet, A. 2010 Rotating helical turbulence. I. Global evolution and spectral behavior. *Phys. Fluids* **22** (3), 035105. 1, 2

Mininni, P. D., Rosenberg, D., Reddy, R. & Pouquet, A. 2011 A hybrid mpi–openmp scheme for scalable parallel pseudospectral computations for fluid turbulence. *Parallel Computing* **37** (6), 316–326. 2

Mishra, Pankaj Kumar, Herault, Johann, Fauve, Stephan & Verma, Mahendra K 2015 Dynamics of reversals and condensates in two-dimensional kolmogorov flows. *Physical Review E* **91** (5), 053005. 5

Moisy, F., Morize, C., Rabaud, M. & Sommeria, J. 2011 Decay laws, anisotropy and cyclone–anticyclone asymmetry in decaying rotating turbulence. *J. Fluid Mech.* **666**, 5–35. 3

Morize, C. & Moisy, F. 2006 Energy decay of rotating turbulence with confinement effects. *Phys. Fluids* **18** (6), 065107. 1, 3

Nazarenko, S. 2011 *Wave turbulence*, , vol. 825. Springer Science & Business Media. 1

Pedlosky, J. 1987 *Geophysical fluid dynamics*. New York, Springer. 1

Pouquet, A. & Marino, R. 2013 Geophysical turbulence and the duality of the energy flow across scales. *Phys. Rev. Lett.* **111** (23), 234501. 1

Pouquet, Annick, Sen, A, Rosenberg, D, Mininni, Pablo Daniel & Baerenzung, J 2013 Inverse cascades in turbulence and the case of rotating flows. *Physica Scripta* **2013** (T155), 014032. 1

Proudman, J. 1916 On the Motion of Solids in a Liquid Possessing Vorticity. *Philos. Trans. R. Soc. London A* **92**, 408–424. 1

Richardson, L. F. 1926 Atmospheric diffusion shown on a distance-neighbour graph. *Proc. Roy. Soc. London. A* **110** (756), 709–737. 6

Roberts, Gareth O 1972 Dynamo action of fluid motions with two-dimensional periodicity. *Philosophical Transactions of the Royal Society of London A: Mathematical, Physical and Engineering Sciences* **271** (1216), 411–454. 2

Ruppert-Felsot, Jori E, Praud, Olivier, Sharon, Eran & Swinney, Harry L 2005 Extraction of coherent structures in a rotating turbulent flow experiment. *Physical Review E* **72** (1), 016311. 1

Scott, Julian F 2014 Wave turbulence in a rotating channel. *Journal of Fluid Mechanics* **741**, 316–349. 1

Sen, A., Mininni, P. D., Rosenberg, D. & Pouquet, A. 2012 Anisotropy and nonuniversality

in scaling laws of the large-scale energy spectrum in rotating turbulence. *Phys. Rev. E* **86** (3), 036319. 1, 2

Seshasayanan, K. & Alexakis, A. 2016 Critical behavior in the inverse to forward energy transition in two-dimensional magnetohydrodynamic flow. *Phys. Rev. E* **93** (1), 013104. 1, 3

Seshasayanan, K., Benavides, S. J. & Alexakis, A. 2014 On the edge of an inverse cascade. *Phys. Rev. E* **90** (5), 051003. 1, 3

Shats, MG, Xia, Hua, Punzmann, Horst & Falkovich, Gregory 2007 Suppression of turbulence by self-generated and imposed mean flows. *Phys. Rev. Lett.* **99** (16), 164502. 3

Smith, L. M., Chasnov, J. R. & Waleffe, F. 1996 Crossover from two-to three-dimensional turbulence. *Phys. Rev. Lett.* **77** (12), 2467. 1

Smith, L. M. & Waleffe, F. 1999 Transfer of energy to two-dimensional large scales in forced, rotating three-dimensional turbulence. *Phys. Fluids* **11**, 1608–1622. 1

Smith R., Leslie M & Yakhot, Victor 1994 Finite-size effects in forced two-dimensional turbulence. *Journal of Fluid Mechanics* **274**, 115–138. 1

Sous, D., Sommeria, J. & Boyer, D. L. 2013 Friction law and turbulent properties in a laboratory Ekman boundary layer. *Phys. Fluids* **25** (4), xx. 6

Sozza, A, Boffetta, G, Muratore-Ginanneschi, P & Musacchio, Stefano 2015 Dimensional transition of energy cascades in stably stratified forced thin fluid layers. *Physics of Fluids* **27** (3), 035112. 1

Sreenivasan, Binod & Davidson, PA 2008 On the formation of cyclones and anticyclones in a rotating fluid. *Physics of Fluids* **20** (8), 085104. 3

Sreenivasan, Katepalli R 1984 On the scaling of the turbulence energy dissipation rate. *The Physics of fluids* **27** (5), 1048–1051. 4

Staplehurst, P. J., Davidson, P. A. & Dalziel, S. B. 2008 Structure formation in homogeneous freely decaying rotating turbulence. *J. Fluid Mech.* **598**, 81–105. 1, 3

Sugihara, Y., Migita, M. & Honji, H. 2005 Orderly flow structures in grid-generated turbulence with background rotation. *Fluid Dyn. Res.* **36**, 23–34. 1

Taylor, G. I. 1917 Motion of Solids in Fluids When the Flow is Not Irrotational. *Proc. R. Soc. London A* **93**, 99–113. 1

Thiele, M. & Müller, W.-C. 2009 Structure and decay of rotating homogeneous turbulence. *J. Fluid Mech.* **637**, 425. 1

Tsang, Y. K. & Young, W. R. 2009 Forced-dissipative two-dimensional turbulence: A scaling regime controlled by drag. *Phys. Rev. E* **79** (4), 045308. 3

Valente, Pedro C & Dallas, Vassilios 2017 Spectral imbalance in the inertial range dynamics of decaying rotating turbulence. *Physical Review E* **95** (2), 023114. 1

Van Bokhoven, LJA, Cambon, Claude, Liechtenstein, Lukas, Godeferd, Fabien S & Clercx, HJH 2008 Refined vorticity statistics of decaying rotating three-dimensional turbulence. *Journal of Turbulence* **9** (N6). 3

van Bokhoven, L. J. A., Clercx, H. J. H., van Heijst, G. J. F. & Trieling, R. R. 2009 Experiments on rapidly rotating turbulent flows. *Physics of Fluids* **21** (9), 096601. 1

Weeks, Eric R, Tian, Yudong, Urbach, JS, Ide, Kayo, Swinney, Harry L & Ghil, Michael 1997 Transitions between blocked and zonal flows in a rotating annulus with topography. *Science* **278** (5343), 1598–1601. 5

Xia, H., Punzmann, H., Falkovich, G. & Shats, M. G. 2008 Turbulence-condensate interaction in two dimensions. *Phys. Rev. Lett.* **101** (19), 194504. 1, 3

Yarom, Ehud & Sharon, Eran 2014 Experimental observation of steady inertial wave turbulence in deep rotating flows. *Nature Physics* **10** (7), 510–514. 1

Yarom, E., Vardi, Y. & Sharon, E. 2013 Experimental quantification of inverse energy cascade in deep rotating turbulence. *Phys. Fluids* **25** (8), 085105. 1

Yeung, P. K. & Zhou, Y. 1998 Numerical study of rotating turbulence with external forcing. *Phys. Fluids* **10** (11), 2895–2909. 1

Yokoyama, N. & Takaoka, M. 2017 Bistability between quasi-two-dimensional flow and three-dimensional flow in forced rotating turbulence. *ArXiv e-prints* , arXiv: 1701.08497. 1, 2, 3, 4, 5, 5

Yoshimatsu, K., Midorikawa, M. & Kaneda, Y. 2011 Columnar eddy formation in freely decaying homogeneous rotating turbulence. *J. Fluid Mech.* **677**, 154–178. 1

Zavala Sansón, L, van Heijst, GJF & Backx, NA 2001 Ekman decay of a dipolar vortex in a rotating fluid. *Phys. Fluids* **13** (2), 440–451. 6

Zeman, O. 1994 A note on the spectra and decay of rotating homogeneous turbulence. *Phys. Fluids* **6** (10), 3221–3223. 1